

High-temperature altered oceanic crust recycling into oceanic-island basalt-like mantle produces alkaline continental crust driven by mélange diapirs: Insights from isotopic tracing and numerical modeling

Huichuan Liu^{1,2}, Pengpeng Huangfu^{3,4,†}, and Guangyou Zhu⁵

¹State Key Laboratory of Petroleum Resources and Prospecting, China University of Petroleum (Beijing), Beijing 102249, China

²College of Geosciences, China University of Petroleum (Beijing), Beijing 102249, China

³Key Laboratory of Computational Geodynamics, College of Earth and Planetary Sciences, University of Chinese Academy of Sciences, Beijing 100049, China

⁴SinoProbe Laboratory of Chinese Academy of Geological Sciences, Beijing 100037, China

⁵Research Institute of Petroleum Exploration and Development, PetroChina, Beijing 100083, China

ABSTRACT

Genesis of the large-volume alkaline crust at active continental margin is still enigmatic for geologists worldwide. The point at issue is whether or not subducted oceanic crusts get involved and how they interact with the mantle source of the alkaline crust. Late Mesozoic juvenile alkaline crusts with high $\varepsilon_{\text{Nd}}(t)$ - $\varepsilon_{\text{Hf}}(t)$ values are widely distributed in the Great Xing'an Range of NE China, as parts of an arc magmatic belt related to the Mongol-Okhotsk Ocean closure. We carried out multi-isotope analyses and 2-D high-resolution numerical modeling to trace the mantle source nature of the alkaline crust. The alkaline rocks show similar trace elements with the I-type enriched mantle and are originated from an upwelling oceanic-island basalt-like mantle. Their high field strength element depleted arc features indicate the crustal material addition in the source region. Low $\delta^{18}\text{O}$, mantle-like Sr-Nd-Hf and light Mg isotope compositions, limited $\delta^7\text{Li}$ variations, no Nd-Hf decoupling, and our mixing calculation preclude continental crustal assimilation, marine-sediment melt and/or altered oceanic crust (AOC)-fluid metasomatism, and bulk marine sediment involvement, and provide evidence of the bulk AOC addition in the mantle source. Lower $\delta^{18}\text{O}$ values than the mantle and relatively low $\delta^7\text{Li}$ values further confirmed the involved AOC to be a high-temperature (high-T) AOC. Our multi-


isotope tracing successfully fingerprints the recycled high-T AOC into the source region of the alkaline juvenile crust. Then, our 2-D high-resolution numerical modeling reconstructs the high-T AOC recycling processes driven by mélange melting.

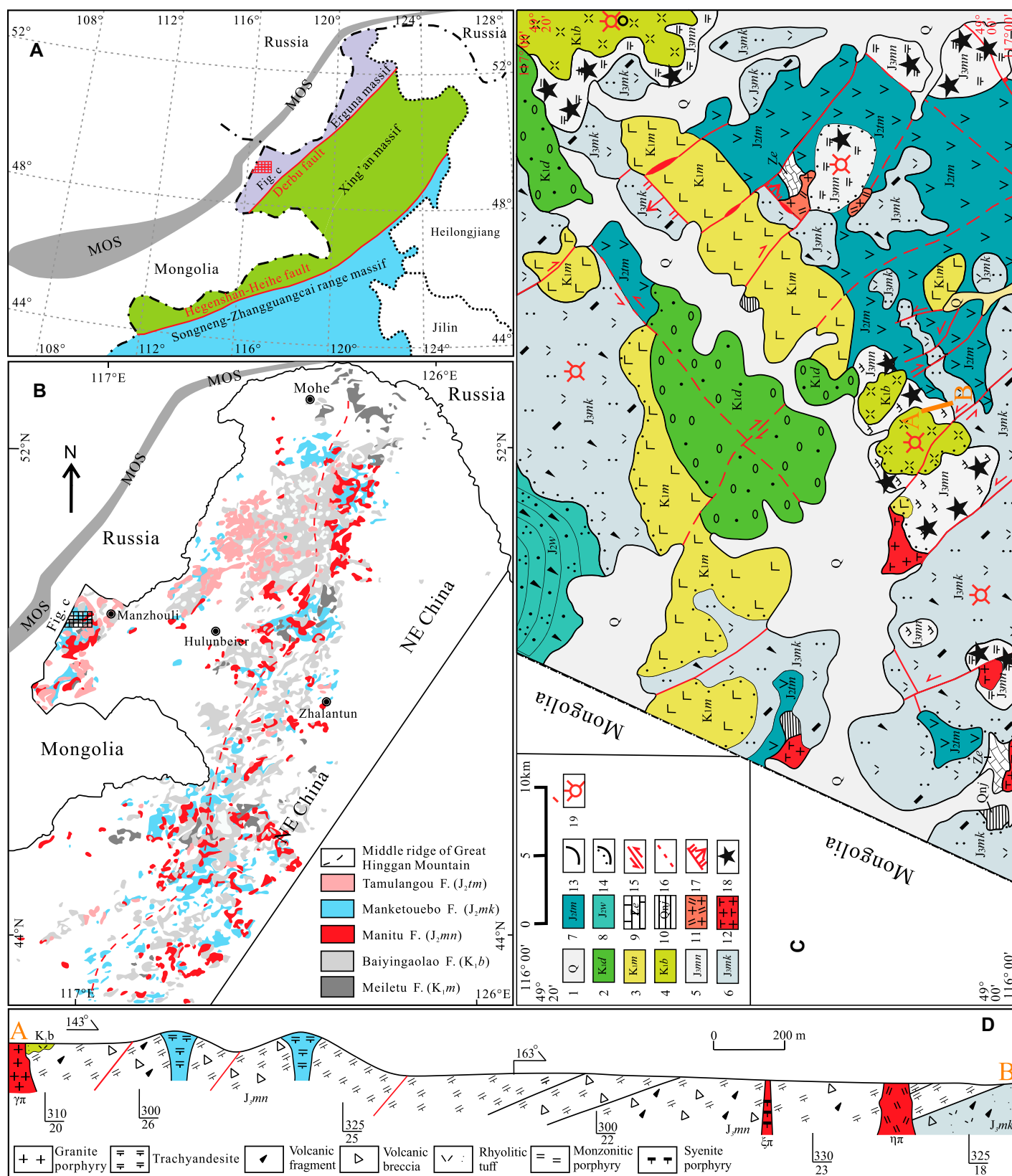
1. INTRODUCTION

Crustal growth is a complicated magmatic process, which extracts material from the upper mantle to Earth's surface (Cawood et al., 2013; Hawkesworth and Kemp, 2006; Rudnick, 1995), and juvenile crust can be divided into subalkaline and alkaline types based on their alkaline element contents. Subalkaline crust is common in all tectonic settings and has been studied extensively (Petford et al., 2000; Rapp et al., 2003). Alkaline crust is characterized by high alkaline element contents, and may occur at continental rift, active continental margin, and mantle plume settings. Alkaline crust is closely associated with some important geological processes, such as mantle plume, crust-mantle interaction, mineralization of rare earth and gold, and carbon cycling (Buono et al., 2020; Pilet et al., 2008), for which probing its genesis is important for global geologists. The point at issue is whether or not crust materials including continental and oceanic crust have been involved and how they interact with the mantle source of the alkaline crust (Cruz-Uribe et al., 2018; Zhu et al., 2017). At an active continental margin setting, the role of subducted oceanic crust in the genesis of alkaline crust is still a pending problem.

Subducted oceanic crust (i.e., subducted mélange) contains marine sediments, altered oceanic crust (AOC), and mantle peridotite

(Codillo et al., 2018; Nielsen and Marschall, 2017). Two different processes have been proposed for the interaction of subducted oceanic crust with the sub-arc mantle: marine sediment melt and/or AOC fluid metasomatism on sub-arc mantle, and physical mixing of subducted mélange with sub-arc mantle (Nielsen and Marschall, 2017). The metasomatized mantle model with sediment melting and AOC and/or serpentinite dehydration has long dominated our understanding of the arc formation processes. However, melting of marine sediment only occurs at temperatures $>1050^\circ\text{C}$ under the pressure of a subduction zone (2.7–5 GPa) (Behn et al., 2011). Such high temperatures cannot be reached at similar pressures along the slab interface with the sub-arc mantle. Thus, geologists worldwide are paying more attention to the mélange mixing models (Codillo et al., 2018; Cruz-Uribe et al., 2018; Little et al., 2011; Nielsen and Marschall, 2017). Mélange mixing models invoke physical mixing of bulk marine sediment and AOC with the sub-arc mantle first, followed by melting and dehydration processes (Ho, 2019; Nielsen and Marschall, 2017; Wu et al., 2020). Recently, combined radiogenic and stable isotopes are widely used to trace the addition of different oceanic components (Hao et al., 2022; Nielsen and Marschall, 2017). For example, due to isotopic fractionation caused by the continental derived particles, sea water reaction, and low oxygen fugacity, marine sediments have high radiogenic Sr-Nd-Hf-Pb isotopes and heavy and variable Mg-Li-O isotopes (Basak et al., 2011; Chan et al., 2006; Hu et al., 2017; Vervoort et al., 2011). AOC can be subdivided into two types: low-temperature ($<150^\circ\text{C}$) and high-temperature ($>150^\circ\text{C}$) AOC. Because of

Pengpeng Huangfu  <https://orcid.org/0000-0001-7651-7653>
†huangfu@ucas.ac.cn



their different water/rock ratios, low-T AOC has significant heavier O and Li isotopes than the high-T AOC (Bindeman et al., 2008; Cerling

et al., 1985; Donoghue et al., 2008; Troch et al., 2020; Zack et al., 2003; Zhao and Zheng, 2003). Thus, rational analyses of multiple isotopes can

be used to trace marine sediment, low-T AOC, and high-T AOC participations in the source regions of the arc rocks.

Figure 1. (A) Tectonic outline of NE China. (B) Spatiotemporal distribution of the middle Mesozoic volcanics in the Erguna and Xing'an massifs of NE China (after (IMBGM, 1991)). (C) Geological map showing the stratigraphic and igneous components of the Aobaowula area (modified from Liu et al., 2019). (D) Cross section of the Manitu Formation at the Aobaowula area. F—Formation; MOS—Mongol-Okhotsk suture; 1—Quaternary; 2—Damoguaihe Formation; 3—Meiletu Formation; 4—Baiyingaolao Formation; 5—Manitu Formation; 6—Manketouebo Formation; 7—Tamulangou Formation; 8—Wanbao Formation; 9—Erguna Formation; 10—Jiageda Formation; 11—Late Jurassic granite; 12—Permian granite; 13—stratigraphic boundary; 14—stratigraphic unconformity; 15—strike-slip fault; 16—inferred fault; 17—normal fault; 18—sample location; 19—volcanic vent.

The Central Asian Orogenic Belt (CAOB), occupying $\sim 8,745,000 \text{ km}^2$ in central and northern Asia, is believed to be the largest area of Phanerozoic crustal growth on Earth (Fig. 1A) (Şengör et al., 2018). The most outstanding feature of the CAOB is the vast expanse of Phanerozoic granitic intrusions and their volcanic equivalents with high $\epsilon_{\text{Nd}}(t) - \epsilon_{\text{Hf}}(t)$ values, which have led to the widely cited conclusion that more than 50% (even up to 80%) of the crust within the CAOB is juvenile (Jahn et al., 2000; Şengör et al., 2018; Zhang et al., 2017; Zhang et al., 2018). Late Mesozoic alkaline igneous rocks are widely distributed in the Great Xing'an Range of the southeastern CAOB and believed to be part of arc rocks related to the southward subduction of the Mongol-Okhotsk Ocean (Figs. 1A and 1B). These widespread alkaline igneous rocks are characterized by high $\epsilon_{\text{Nd}}(t) - \epsilon_{\text{Hf}}(t)$ isotope compositions and represent late Mesozoic juvenile crust (Liu et al., 2019; Zhang, 2014). In this study, we report Sr-Nd-Pb-Hf-O-Mg-Li isotope analyses on Late Jurassic alkaline volcanic rocks in the Great Xing'an Range (Fig. 1C) and two-dimensional (2-D) high-resolution numerical modeling to fingerprint the recycled oceanic materials (marine sediment, low-T AOC, or high-T AOC) in the mantle source and unveil their possible recycling mechanism in a paleo-subduction zone.

2. REGIONAL GEOLOGICAL BACKGROUND AND SAMPLE DESCRIPTIONS

The amalgamation of Siberian, Tarim, and North China cratons during late Paleozoic to early Mesozoic built up the world famous CAOB through a gigantic accretionary orogeny associated with the Paleo-Asian Ocean closure (Xiao et al., 2015). NE China is located in the southeastern section of the CAOB, and consists of a collage of microcontinental massifs, including the Khanka, Jiamusi, Songnen-Zhangguangcai Range, Xing'an, and Erguna massifs (Fritzell et al., 2016). This area has been jointly influenced by the Paleo-Asian Ocean closure and the Paleo-Pacific and Mongol-Okhotsk subductions. The Mongol-Okhotsk suture crops out mainly in Russia and Mongolia based on the studies of the Adaatsag ophiolite in central Mongolia

(325 Ma) and Late Carboniferous oceanic-island basalt with pelagic radiolarian chert in the Gorkhi Formation (Ruppen et al., 2014; Tomurtogoo et al., 2005). Four phases of Late Permian to Early Jurassic magmatic activities (ca. 246 Ma, ca. 225 Ma, ca. 205 Ma, and ca. 185 Ma) and the late Mesozoic Great Xing'an Range large igneous province were identified in the Erguna and Xing'an massifs and related to the Mongol-Okhotsk Ocean southward subduction (Liu et al., 2018; Zhang, 2014). These magmatic records delineated a late Paleozoic to Mesozoic arc-trench system in NE China, which, in combination with previous metamorphic and palaeomagnetic age data, suggest that the Mongol-Okhotsk ocean finally closed during latest Early Cretaceous (Fritzell et al., 2016). Multiple late Mesozoic volcanic rocks and clastic sedimentary rocks are widespread in the Erguna and Xing'an massifs, including the Tamulangou (J_2^{tm}), Manketouebo (J_3^{mk}), Manitu (J_3^{mn}), Baiyingaolao (K_1^b), and Meiletu (K_1^m) formations (Fig. 1C).

The Manitu Formation rests conformably on the Manketouebo Formation and is unconformably overlain by the Baiyingaolao Formation (Fig. 1D). It preserves the most typical late Mesozoic volcanic rocks in NE China, and is composed of andesite, trachyandesite, trachyte, dacite, andesitic breccia, and detritus crystal tuff (Fig. 1D). In this study, we carried out detailed investigations on the Manitu Formation in the Erguna massif (Figs. 1C and 1D), collected all types of the volcanic rocks of the Manitu Formation (Fig. S1¹), and presented their U-Pb ages and element and isotope data.

3. GEOCHRONOLOGICAL AND GEOCHEMICAL CHARACTERISTICS

Zircon U-Pb dating, whole rock element, in situ zircon Lu-Hf-O isotope, and whole rock Sr-Nd-Hf-Mg-Li isotope analyses were carried out

¹Supplemental Material. Supplemental Texts S1–S9: Analytical methods. Supplemental Tables S1–S7: Analytical results. Supplemental Figures S1–S5: Supporting figures. Please visit <https://doi.org/10.1130/GSAB.S.23412545> to access the supplemental material, and contact editing@geosociety.org with any questions.

on the 17 samples from the Manitu Formation. Analytical methods are described in Supplemental Texts S1–S8 and results are listed in Supplemental Tables S1–S4.

3.1. Zircon U-Pb Dating and In Situ Lu-Hf-O Isotopes

Sample TW3933 was collected for laser ablation–inductively coupled plasma–mass spectrometry zircon U-Pb dating (Table S1; Fig. 2). Thirty-one analyses were performed on 31 zircons. Zircon grains were mostly euhedral, transparent to colorless, and stubby to elongate in shape with lengths of 100–150 μm and widths of 60–90 μm (Fig. 2A). Backscattered electron and cathodoluminescence images of all grains display well-preserved euhedral growth zones, with unperturbed oscillatory zoning, typical of igneous zircon (Hanchar and Miller, 1993). All the analyses document much higher Th/U ratios than 0.1 (Fig. 2B), also reflective of an igneous origin. One analysis (TW3933.23) yields a $^{206}\text{Pb}/^{238}\text{U}$ age of 2164 Ma, interpreted as the result of inheritance. Seven spots are obviously discordant and give much older $^{207}\text{Pb}/^{235}\text{U}$ ages. Excluding these eight analyses, the remaining 23 analyses form a homogenous cluster and yield a weighted mean $^{206}\text{Pb}/^{238}\text{U}$ age of $160.8 \pm 1.4 \text{ Ma}$ (mean square of weighted deviates = 2.4, $n = 23$; Fig. 2C). This age (161 Ma) is interpreted as the crystalline age of the Manitu volcanics. We then carried out 20 in situ Lu-Hf-O isotope analyses. The $\delta^{18}\text{O}$ values range from +3.56‰ to +5.12‰, and the $\epsilon_{\text{Hf}}(t)$ values range from +3.9 to +10.8 (Fig. 3; Table S2).

3.2. Whole-Rock Elements

Seventeen volcanic samples show large variations of major and trace element contents (Table S3); e.g., $\text{SiO}_2 = 54.9\text{--}70.8 \text{ wt\%}$. Most samples fall in the alkaline series in the discriminant diagrams (Fig. S2). Samples have high total rare earth element (REE) contents and similar light REE-enriched chondrite-normalized REE patterns and primitive mantle-normalized spidergrams with the oceanic-island basalt (OIB), except the moderately negligible Nb-Ta anomalies (Fig. S3).

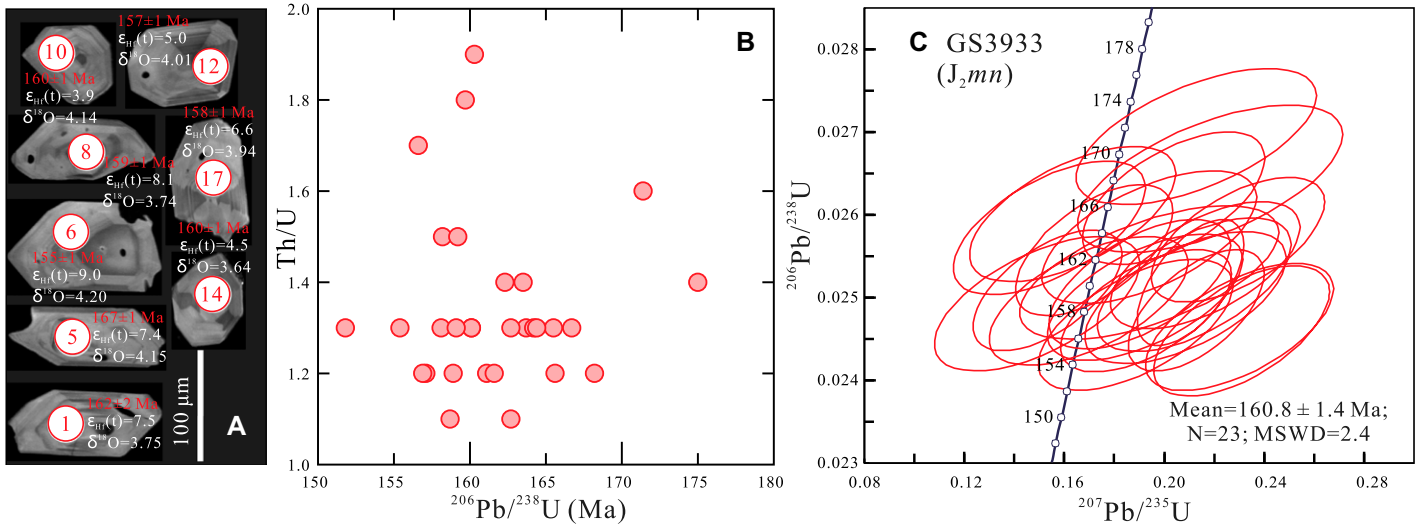


Figure 2. (A) Cathodoluminescence images of the representative zircon grains. (B) Th/U ratios versus $^{206}\text{Pb}/^{238}\text{U}$ apparent ages plots. (C) Laser ablation-inductively coupled plasma-mass spectrometry zircon U-Pb concordia diagrams for the volcanic samples from the Manitu volcanic rocks in NE China. White circles on cathodoluminescence images mark analytical site on each grain. MSWD—mean square of weighted deviates.

3.3. Whole-Rock Sr-Nd-Hf-Pb-Mg-Li Isotopes

Initial Sr, Nd, and Hf isotopic ratios are recalculated to the crystallization age of 161 Ma (Table S4). Manitu samples have $(^{87}\text{Sr}/^{86}\text{Sr})_i$ ratios of 0.70477–0.70518, $\epsilon_{\text{Nd}}(t)$ values of +1.1 to +1.5, and $\epsilon_{\text{Hf}}(t)$ values of +5.0 to +6.0 (Figs. 4A and 4B). Their $(^{206}\text{Pb}/^{204}\text{Pb})_i$, $(^{207}\text{Pb}/^{204}\text{Pb})_i$, and $(^{208}\text{Pb}/^{204}\text{Pb})_i$ ratios range from 18.36 to 18.45, 15.55 to 15.56, and 38.51 to 38.57, respectively (Table S4). On $(^{206}\text{Pb}/^{204}\text{Pb})_i$

versus $(^{208}\text{Pb}/^{204}\text{Pb})_i$ and $(^{207}\text{Pb}/^{204}\text{Pb})_i$ geochemical diagrams, all samples plot slightly above the North Hemisphere Reference Line (Figs. 4C and 4D). The Manitu samples have $\delta^{26}\text{Mg}$ values of -0.168‰ to 0.009‰ , and $\delta^7\text{Li}$ values of 4.94‰ to 5.49‰ (Table S4; Fig. 5).

4. NUMERICAL MODELING

In order to better explicate the dynamics of mélangé diapir and AOC recycling, 2-D high-resolution numerical modeling was conducted

to reproduce the ascending processes of subducted mélangé. With the thermo-mechanical code “I2VIS” (Gerya and Yuen, 2003, 2007), a numerical model ($4000\text{ km} \times 670\text{ km}$; Fig. 6) representing the ocean-continent subduction system was built. The model consists of non-uniform 699×134 rectangular grids with a resolution varying from $2\text{ km} \times 2\text{ km}$ in the collision zone to $30\text{ km} \times 30\text{ km}$ close to the boundary. A 2000-km-long oceanic domain and a 2000-km-long continental domain comprise the model, which are separated by a weak zone aiming to initiate oceanic subduction. The oceanic and continental lithospheres in this study are separately set to be 76 km thick and 120 km thick, with the initial thickness of oceanic crust, continental upper crust, and continental lower crust being 8 km, 20 km, and 15 km, respectively. The flow law of wet quartzite is applied to sediments and continental upper crust, and the flow law of plagioclase to oceanic crust and continental lower crust. Both the lithospheric mantle and the subjacent asthenosphere are represented by dry olivine. The details of the numerical methodology and model configurations can be found in Supplemental Text S9.

The model results show that at a convergence velocity of 3 cm/yr, the rigid oceanic plate steadily subducts along the weak zone and sinks into the asthenosphere (Fig. 7). Continued subduction of the oceanic plate triggers three-phase mélangé upwelling into the mantle wedge: (1) marine sediment diapir, (2) mélangé diapir (including both marine sediment and AOC), and (3) AOC diapir. Owing to the large positive buoyancy, a substantial portion of the subducted marine sediments is

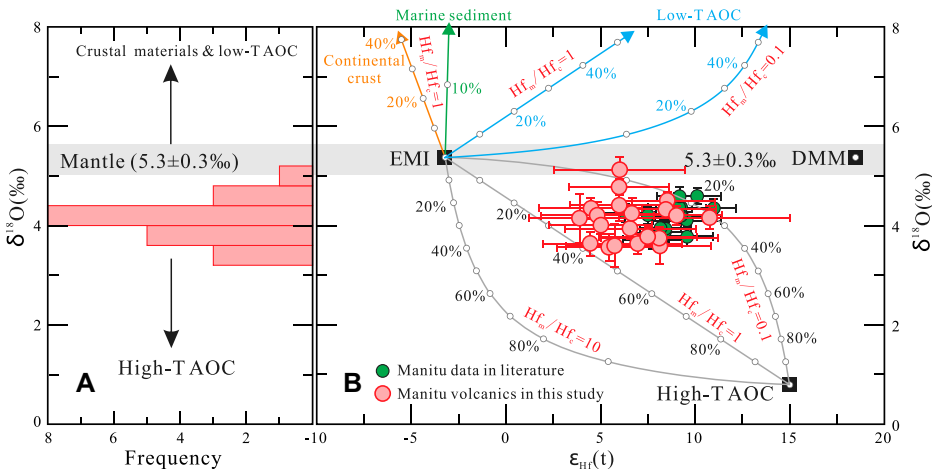


Figure 3. Zircon in situ Hf-O isotope compositions of the Manitu volcanic rocks in NE China. (A) Relative probability plots of zircon in situ $\delta^{18}\text{O}$ values, and (B) plots of zircon in situ $\epsilon_{\text{Hf}}(t)$ versus $\delta^{18}\text{O}$ and mixing modeling results. The mixing end members and associated references are listed in Table S5 (see text footnote 1). T—temperature; High-T AOC—high-temperature altered oceanic crust; Low-T AOC—low-temperature altered oceanic crust; EMI—I-type enriched mantle; DMM—depleted mid-oceanic-ridge basalt (MORB)-type mantle.

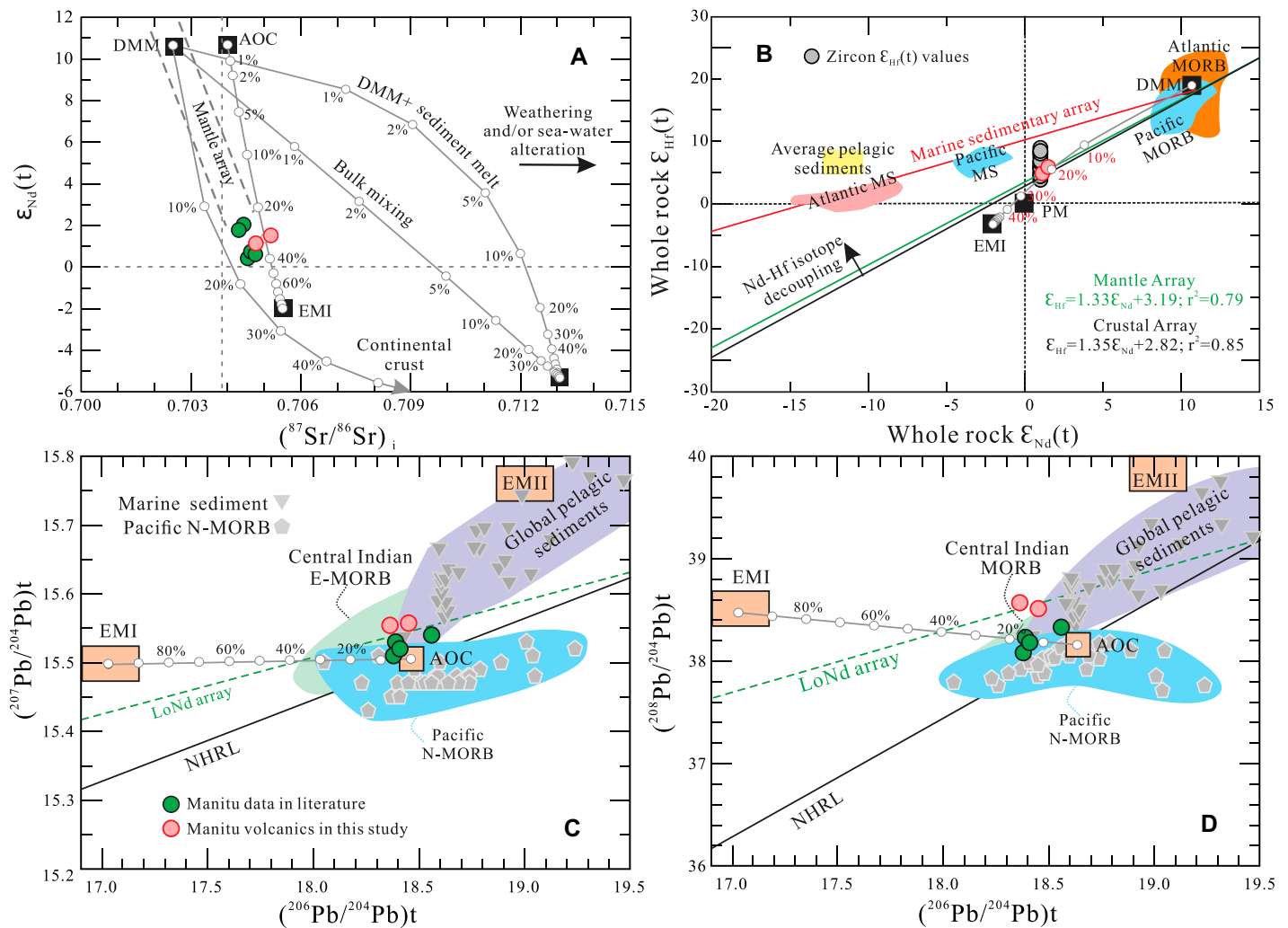


Figure 4. (A) Nd-Sr isotope correlation and mixing modeling results. (B) Plot of Nd isotopes versus Hf isotopes and mixing modeling results. (C and D) Plots of $^{206}Pb/^{204}Pb$ versus $^{207}Pb/^{204}Pb$ and $^{208}Pb/^{204}Pb$ for the Manitu volcanic rocks in NE China. The mixing end members and associated references are listed in Table S5 (see text footnote 1). AOC—altered oceanic crust; EMI—I-type enriched mantle; DMM—depleted MORB-type mantle; MORB—mid-oceanic-ridge basalt; N-MORB—normal MORB; MS—marine sediment; PM—primitive mantle; NHRL—Northern Hemisphere Reference Line.

immediately delaminated from the oceanic slab and accumulates at the bottom of the overriding continental lithosphere, when just sinking into the asthenosphere (Fig. 7A). The delaminated sediments experience intensive melting, which is accompanied by landward advance of the partial melts and the enclosed oceanic crust. Meanwhile, such progressive melt flow significantly erodes and mechanically thins the overriding lithospheric mantle, favoring further episodes of lithospheric-scale diapirs. At a greater depth, the increased density contrast between the subducting oceanic crust and the surrounding mantle promotes upward delamination of the oceanic crust from the descending slab. During the early term, the residual marine sediments are separated together with the oceanic crust, leading to a mélangé (including

both marine sediment and AOC) diapir (Fig. 7B). Subsequently, considerable diapiric flows, due to crustal Rayleigh-Taylor instabilities at the top of the cold subducting slab, develop and prevail in the mantle wedge (Fig. 7C). These upward cold plumes are lubricated by viscous heating and are greatly fueled by partial melting of the ascending oceanic crust during its rise, driven by compositional buoyancy (Fig. 7C).

5. DISCUSSION

5.1. Effects of Fractional Crystallization and Crustal Assimilation

Lowest SiO_2 content of the Manitu volcanic rocks is 54.9 wt%, and thus, they cannot have

been derived exclusively from continental crust melting. The Manitu samples show variable SiO_2 contents of 54.9–70.8 wt%. Such a large range of SiO_2 content could be produced by fractional crystallization, crustal assimilation, or various degrees of partial melting. Major and trace elements of our samples show a strong correlation with the SiO_2 contents (Fig. S4), indicating significant fractional crystallization in their petrogenesis. One xenolithic zircon from the dated sample may have been inherited from minor assimilation of sedimentary rocks, but the following observations argue against significant continental material contributions. (1) Continental materials are generally calc-alkaline and enriched in K relative to Na. Our samples are silica-oversaturated alkaline rocks

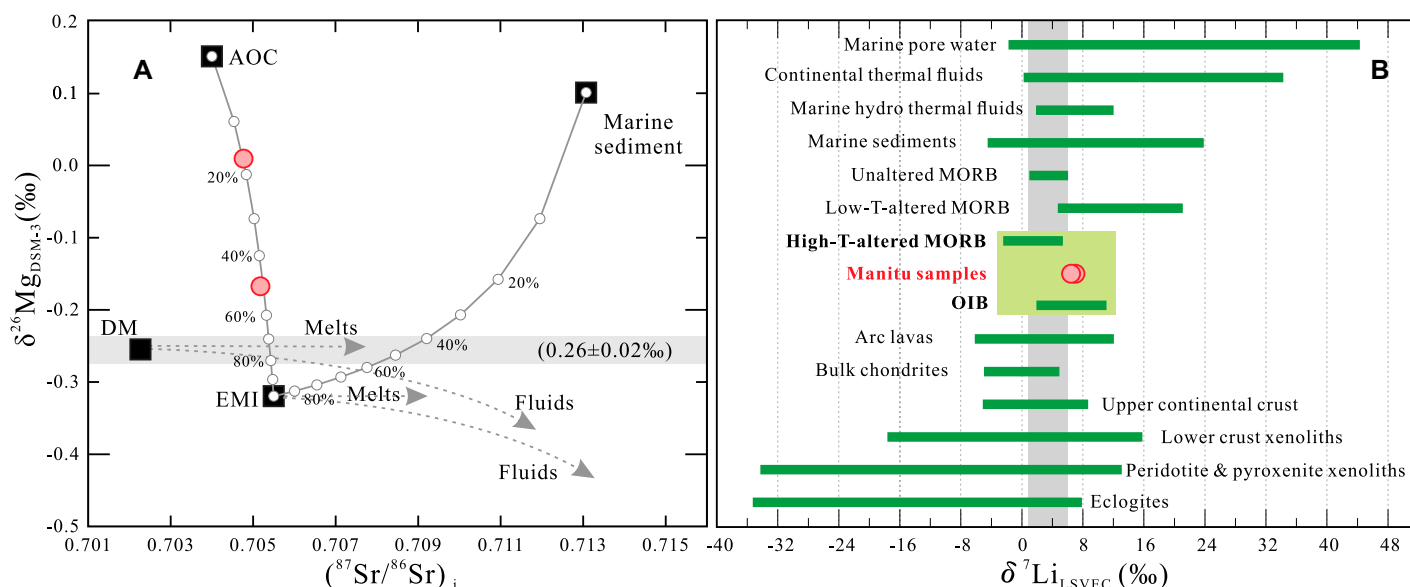


Figure 5. (A) Plots of $(^{87}\text{Sr}/^{86}\text{Sr})_i$ versus $\delta^{26}\text{Mg}$, and (B) compilation of whole-rock Li isotopic compositions of various rock types and water. The fields of EM1, EM2, and marine sediments in Figure 5A are from Hart et al. (1986), Hu et al. (2017), Huang et al. (2018), Plank et al. (2007), Weaver (1991), and Zhong et al. (2017), and mixing end members and associated references are listed in Table S5 (see text footnote 1). For the detailed data sources of Figure 5B, please refer to Tang et al. (2010). T—temperature; AOC—altered oceanic crust; EMI—I-type enriched mantle; DM—depleted mantle; MORB—mid-oceanic-ridge basalt; OIB—oceanic-island basalt; LSVEC—international standard with an absolute $^6\text{Li}/^7\text{Li}$ abundance ratio of 0.0832 ± 0.0002 .

and have high Na_2O contents and high $\text{Na}_2\text{O}/\text{K}_2\text{O}$ ratios (Fig. S5A). (2) Our samples have lower $\delta^{18}\text{O}$ values of $+3.56\text{‰}$ to $+5.12\text{‰}$ than the mantle array ($+5.3\text{‰} \pm 0.3\text{‰}$), in contrast to the high $\delta^{18}\text{O}$ values (up to 20‰) of continental materials. (3) Significant crustal assimilation would produce highly radiogenic Sr and Pb isotope values, which are not observed in the Manitu volcanics (Fig. 4). (4) Our samples

have high whole-rock $\epsilon_{\text{Nd}}(t)$ ($+1.1$ to $+1.5$), $\epsilon_{\text{Hf}}(t)$ ($+5.0$ to $+6.0$), and zircon $\epsilon_{\text{Hf}}(t)$ ($+3.9$ to $+10.8$) values, even higher than primary mantle (Figs. 3 and 4B). (5) Crustal contamination, if any, might decrease the Nb/La ratios, resulting in a positive correlation between MgO and Nb/La ratios. No such correlations have been observed in our samples (Fig. S5B). Therefore, the variable element compositions of the Manitu

volcanics can only result from various degrees of partial melting of mantle sources.

5.2. An Upwelling OIB-like Mantle Origin for the Manitu Alkaline Volcanics

For the alkaline basalts from ocean islands and continents, three different origins have been proposed by previous studies: recycled oceanic

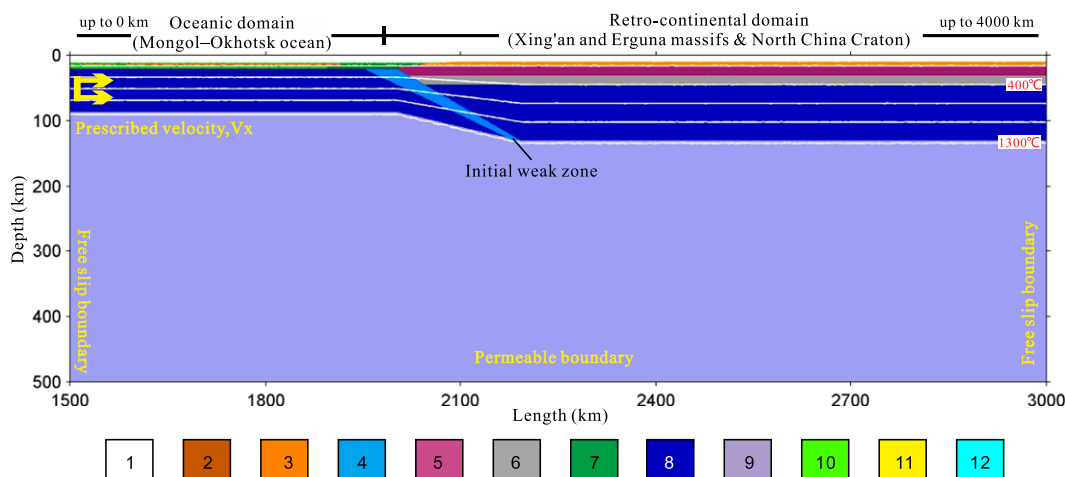


Figure 6. Initial model configurations. Enlargement ($1500 \times 500 \text{ km}$) of the numerical box ($4000 \times 670 \text{ km}$) is shown. White lines are isotherms with an interval of 300°C . Two different lithospheres comprise the model, with oceanic on the left and continental on the right. A rightward velocity of 3 cm/yr is assigned within the oceanic lithosphere. Different colors refer to different lithologies, with: 1—air; 2/3—sediments; 4—weak zone; 5—continental upper crust; 6—continental lower crust; 7—oceanic crust; 8—lithospheric mantle; 9—asthenospheric mantle; 10—partially molten oceanic crust; 11—partially molten marine sediments; 12—sea-water. The partially molten crustal rocks (10 and 11) will appear during the evolution of the model (Fig. 7). Detailed properties of different rock types are shown in Tables S6 and S7 (see text footnote 1).

8—lithospheric mantle; 9—asthenospheric mantle; 10—partially molten oceanic crust; 11—partially molten marine sediments; 12—sea-water. The partially molten crustal rocks (10 and 11) will appear during the evolution of the model (Fig. 7). Detailed properties of different rock types are shown in Tables S6 and S7 (see text footnote 1).

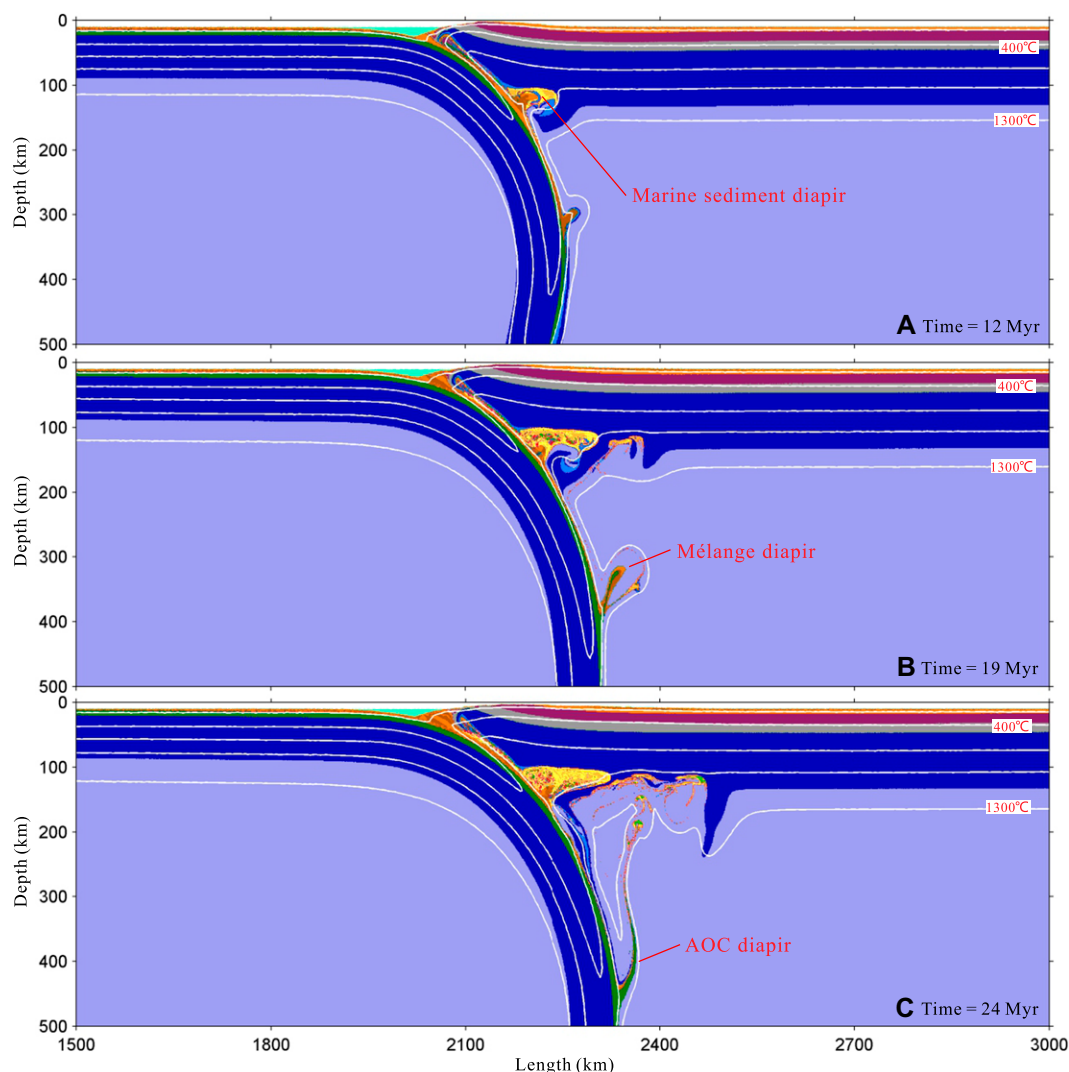


Figure 7. Evolution of the numerical model with a convergence velocity of 3 cm/yr. Composition evolution is overlapped by white-line isotherms, which are plotted every 300 °C starting from 100 °C. Colors of rock types are the same as in Figure 6. AOC—altered oceanic crust.

crust with or without sediment (Cruz-Urbe et al., 2018; Hofmann, 1997), subcontinental lithospheric mantle (Pilet et al., 2008; Xu et al., 2017), and upwelling OIB-like asthenosphere mantle (Ruttur et al., 2021; Xu et al., 2005). Oceanic crust has low radiogenic Sr and high radiogenic Pb, Nd, and Hf isotopes, and its partial melt will inherit these isotope compositions, i.e., low $(^{87}\text{Sr}/^{86}\text{Sr})_i$ ratios, high $\varepsilon_{\text{Nd}}(t)$ and $\varepsilon_{\text{Hf}}(t)$ values, and high $(^{206}\text{Pb}/^{204}\text{Pb})_i$, $(^{207}\text{Pb}/^{204}\text{Pb})_i$, and $(^{208}\text{Pb}/^{204}\text{Pb})_i$. Partial melting of young oceanic crust will produce adakitic magma with high Sr contents and high Sr/Y ratios. Our Manitu samples have distinctively different Sr, Nd, and Hf isotopes (Fig. 4) and Sr/Y ratios from the oceanic crust (Fig. S5C). Stable isotopes in the mantle will be homogenized after long-term preservation. Subcontinental lithospheric mantle will hold similar O and Mg isotopes with normal mantle (i.e., $\delta^{18}\text{O} = +5.3\text{‰} \pm 0.3\text{‰}$ and $\delta^{26}\text{Mg} = +0.26\text{‰} \pm 0.02\text{‰}$), and its partial

melting cannot produce the low $\delta^{18}\text{O}$ and high $\delta^{26}\text{Mg}$ of our samples (Figs. 4 and 5). Upwelling OIB-like mantle derived magma has I-type enriched mantle (EMI)-like geochemical features, such as Hawaiian OIB (Sobolev et al., 2011) and Emeishan high-Ti basalt (Xu et al., 2001). The Manitu volcanics show similar trace element spidergrams and REE patterns with OIB, except the Nb-Ta negative anomalies, and plot approaching to the EMI on the Sr-Nd-Hf isotope correlation diagrams (Figs. 4A and 4B). Thus, the Manitu volcanics are likely to have originated from an upwelling OIB-like mantle.

However, in comparison with the typical OIB, the Manitu volcanics feature significant Nb-Ta negative anomalies on the trace element spidergrams (Fig. S3A). These features could be produced by continental crust contamination, subducted melt and/or fluid metasomatism, and subducted mélangé mixing. Our aforementioned discussion has precluded significant crustal con-

tamination. Sediment melts and AOC fluids display similar Sr-Nd isotope compositions and much lower Nd/Sr ratios than their respective bulk counterparts (marine sediment and AOC). Mixing curves of these components in Sr-Nd isotope space have very different curvatures from those dominated by the mixing of bulk sediment and bulk AOC (Fig. 4A) (Nielsen and Marschall, 2017). We performed binary mixing calculations using bulk marine sediment and AOC and sediment melts and AOC fluids as end members, respectively, as shown in Figure 4A. Our samples plot along the mixing lines between bulk EMI and bulk AOC, far away from those of sediment melts and AOC fluids. Aqueous Mg^{2+} in subduction zones is enriched in lighter Mg isotope compositions (Wang et al., 2019), and the AOC fluid and sediment melt typically show much lower $\delta^{26}\text{Mg}$ values (down to -1.3‰) than mantle peridotites (Chen et al., 2018). In contrast, our Manitu samples have heavier

$\delta^{26}\text{Mg}$ values than those of OIB (Zhong et al., 2017), arc rocks (Teng et al., 2016), and mid-oceanic-ridge basalt (MORB) (Liu et al., 2017) (Fig. 5A). AOC fluid and sediment melt metasomatism is excluded. Experimental studies (Cruz-Uribe et al., 2018) have confirmed that partial melting of the *mélange* diapir with variable contributions from sub-arc mantle, AOC, and sediments can produce alkaline arc melts. Previous natural *mélange* rock investigation and piston-cylinder experiments (Codillo et al., 2018; Ho, 2019) found that selective retention of high field strength elements (HFSE) by some accessory minerals (e.g., rutile, sphene, and perovskite) stabilized in the sub-arc mantle and/or in the slab can attributed to the depleted HFSE features of the arc rocks (Hermann and Rubatto, 2009). Thus, subducted *mélange* mixing dominates the alkaline and arc geochemical compositions of the Manitu volcanics. Subducted *mélange* is composed of marine sediments and AOC, and the AOC could be subdivided into high-T and low-T subtypes. Which component has been assimilated into the source region is still a pending problem.

5.3. High-T AOC Recycling into Upwelling OIB-Like Mantle

The isotope features of the Manitu samples argue against marine sediment involvements. (1) Marine sediments tend to absorb heavy oxygen isotopes and have much higher $\delta^{18}\text{O}$ values than the mantle, which are distinctively different from the lower $\delta^{18}\text{O}$ values in our samples (Fig. 3). (2) Marine sediments commonly preserve radiogenic Sr-Nd-Pb isotopes, and show higher ($^{87}\text{Sr}/^{86}\text{Sr}$), ($^{206}\text{Pb}/^{204}\text{Pb}$), ($^{207}\text{Pb}/^{204}\text{Pb}$), and ($^{208}\text{Pb}/^{204}\text{Pb}$) ratios and lower $\varepsilon_{\text{Nd}}(t)$ values than our samples. The Manitu samples plot far away from the mixing lines between the marine sediments and the mantle (Fig. 4). (3) Significant marine sediment addition results in Nd-Hf decoupling (Chauvel et al., 2008; Zhang et al., 2020), meaning that the $\varepsilon_{\text{Nd}}(t)$ and $\varepsilon_{\text{Hf}}(t)$ values plot far from the terrestrial array (Vervoort et al., 2011). Our samples fall along the mantle and crustal arrays in Figure 4B. (4) Marine sediments have a large range of $\delta^7\text{Li}$ values (-5‰ to 24‰), and their participation in a source region will produce variable Li isotope compositions in the magma, distinct from our Manitu samples (Fig. 5B). In contrast, on all the isotope correlation diagrams the Manitu samples plot along the mixing lines between the AOC and EMI (Figs. 3–5). Thus, AOC is the main factor affecting elemental and isotope compositions of the Manitu volcanics.

One outstanding problem is that the AOC is low-temperature ($<150\text{ °C}$) or high-temperature ($>150\text{ °C}$). Due to the large fractionation of

oxygen isotopes between rock and water at low temperatures [e.g., $\Delta^{18}\text{O}(\text{granite-H}_2\text{O}) > 10\text{‰}$ at 150 °C ; Zhao and Zheng, 2003], low-temperature alteration would lead to high $\delta^{18}\text{O}$ in the altered rock, even when meteoric water with low $\delta^{18}\text{O}$ values is involved (Cerling et al., 1985; Donoghue et al., 2008). On the other hand, efficient lowering in the $\delta^{18}\text{O}$ value of the altered rock requires isotope exchange with isotopically light water at elevated temperatures, where isotope fractionation is small; e.g., $\Delta^{18}\text{O}(\text{granite-H}_2\text{O}) < 2\text{‰}$ at 450 °C (Troch et al., 2020; Zhao and Zheng, 2003). Surface water, i.e., meteoric and sea water, is the only reservoir on Earth with $^{18}\text{O}/^{16}\text{O}$ ratios significantly lower than MORB (Bindeman et al., 2008). The oxygen exchange must occur during high-temperature alteration, in order for hydrothermally altered rocks to approach the $\delta^{18}\text{O}$ value of the altering fluid (Troch et al., 2020). Therefore, high-T AOC has lighter (Troch et al., 2020), but low-T AOC has heavier, oxygen isotopes (Staudigel et al., 1995) than the mantle (Fig. 3). The Manitu samples have lower $\delta^{18}\text{O}$ values of $+3.69\text{‰}$ to $+5.22\text{‰}$ than the mantle, and plot on the mixing lines between EMI and high-T AOC, far away from the low-T AOC. Besides, low-T AOC has higher and more variable $\delta^7\text{Li}$ values than the high-T AOC (Zack et al., 2003), and only the mixing of high-T AOC with OIB-like mantle can account for the relatively low $\delta^7\text{Li}$ values of the Manitu volcanics (Fig. 5B).

5.4. Numerical Constraints on the Upwelling Processes of *Mélange* Diapir

Mantle wedge diapirs have been observed by a dense seismic array in Northern Taiwan (Lin et al., 2021). The numerical modeling in this study reproduced the ascending processes of subducted *mélange* and recognized the physical mechanism for the *mélange* diapir and AOC recycling as well as the controlling factor. The model results suggest three phases of diapiric flow in the mantle wedge above the subducting slab, which are manifested by substantial marine sediment melting and diapir at the base of the overriding lithospheric mantle, rising of *mélange* (comprising both marine sediment and AOC), and prevailing Rayleigh-Taylor instabilities of the AOC in the sequence of time and space (Fig. 7). All the three-phase diapirs are fundamentally driven by the compositional buoyancy and accompany extensive partial melting of the oceanic sediments and crust during rising.

Previous studies revealed that when the amplitude of the buoyancy-induced instability exceeds the initial thickness of the sediment layer along the slab top pressure-temperature-time path, a *mélange* diapir develops (Ho, 2019). Any sedi-

ment layer thicker than $\sim 100\text{ m}$ will become unstable on time scales shorter than 1 m.y. at a temperature of 1000 °C (Behn et al., 2011). Within the hot corner of the mantle wedge, more extreme temperatures in excess of 1300 °C are estimated (Currie and Hyndman, 2006; Kelley et al., 2010). The subducted marine sediments have the lowest density among the *mélange* components that are more buoyant than the overlying mantle wedge. For both warm and cold slab-top geotherms, the density contrast between the overlying mantle and the average ultra-high pressure metapelite is as much as -200 kg/m^{-3} for all pressures up to 6 GPa (Behn et al., 2011). Hence, with continued subduction of the oceanic plate, the marine sediments upwell firstly from the downgoing slab (Fig. 7A). Despite the higher density of the marine sediments, the *mélange* rocks, a mixture of the marine sediments and AOC, remain buoyant with respect to the surrounding mantle materials, leading to its subsequent upwelling into the overlying mantle wedge (Fig. 7B). Although average density (3.0 g/cm^3) of fresh oceanic crust is lower than the mantle wedge ($\sim 3.2\text{ g/cm}^3$), their viscosity contrast hinders fresh oceanic crust upwelling along the interface between the subducting slab and overlying mantle. High-T alteration will decrease the density of oceanic crust. For example, serpentinites produced by serpentinization of olivine and pyroxene at $200\text{--}400\text{ °C}$ have much lower density of 2.57 g/cm^3 than fresh oceanic crust and mantle wedge. Such sharp density contrasts between the high-T AOC and mantle wedge after long-term ($\sim 24.7\text{ m.y.}$) subduction of the oceanic plate make the AOC diapir formation and rise up possible (Fig. 7C).

In summary, continued subduction promotes extensive melting of the subducted marine sediment at the bottom of the overriding continental lithosphere as well as long-lived upward delamination of the oceanic crust from the sinking slab (Fig. 7C). This process is accompanied with substantial recycling of high-T altered oceanic crust into the overriding mantle wedge, which is suggested to eventually contribute to considerable alkaline continental crust in the southeastern CAOB driven by *mélange* diapirs.

6. CONCLUSIONS

(1) Low $\delta^{18}\text{O}$, mantle-like Sr-Nd-Hf and light Mg isotope compositions, no Nd-Hf decoupling, and our mixing calculation provide evidence of the bulk AOC addition into OIB-like mantle, which produced large-scale alkaline continental crust in the SE Central Asian Orogenic Belt driven by *mélange* melting. Lower $\delta^{18}\text{O}$ values than the mantle and relatively low $\delta^7\text{Li}$ values further confirm the involved AOC to be high-T AOC.

(2) 2-D high-resolution numerical modeling substantiates the mélange diapir upwelling and high-T AOC recycling processes into the mantle wedge in a subduction zone.

ACKNOWLEDGMENTS

Huichuan Liu thanks the National Key R&D Program of China (grant no. 2021YFA0719000) and Science Foundation of China University of Petroleum, Beijing, China (grant no. 2462018YJRC030) for financial support. Pengpeng Huangfu received support from the National Natural Science Foundation of China (grant nos. 42030307 and 42074107), Open Fund from SinoProbe Laboratory (grant no. SinoProbe Lab 202205), and the Fundamental Research Funds for the Central Universities.

REFERENCES CITED

- Basak, C., Martin, E.E., and Kamenov, G.D., 2011, Seawater Pb isotopes extracted from Cenozoic marine sediments: *Chemical Geology*, v. 286, p. 94–108, <https://doi.org/10.1016/j.chemgeo.2011.04.007>.
- Behn, M.D., Kelemen, P.B., Hirth, G., Hacker, B.R., and Massonne, H.J., 2011, Diapirs as the source of the sediment signature in arc lavas: *Nature Geoscience*, v. 4, p. 641–646, <https://doi.org/10.1038/ngeo1214>.
- Bindeman, I., Brooks, C., McBirney, A., and Taylor, H., 2008, The low- $\delta^{18}\text{O}$ late-stage ferrodiorite magmas in the Skaergaard Intrusion: Result of liquid immiscibility, thermal metamorphism, or meteoric water incorporation into magma?: *The Journal of Geology*, v. 116, p. 571–586, <https://doi.org/10.1086/591992>.
- Buono, G., Fanara, S., Macedonio, G., Palladino, D.M., Petrosino, P., Sottili, G., and Pappalardo, L., 2020, Dynamics of degassing in evolved alkaline magmas: Petrological, experimental and theoretical insights: *Earth-Science Reviews*, v. 211, <https://doi.org/10.1016/j.earscirev.2020.103402>.
- Cawood, P.A., Hawkesworth, C.J., and Dhuime, B., 2013, The continental record and the generation of continental crust: *Geological Society of America Bulletin*, v. 125, p. 14–32, <https://doi.org/10.1130/B30722.1>.
- Cerling, T.E., Brown, F.H., and Bowman, J.R., 1985, Low-temperature alteration of volcanic glass: Hydration, Na, K, ^{18}O and Ar mobility: *Chemical Geology*, v. 52, p. 281–293.
- Chan, L.H., Leeman, W.P., and Plank, T., 2006, Lithium isotope composition of marine sediments: *Geochemistry, Geophysics, Geosystems*, v. 7, <https://doi.org/10.1029/2005GC001202>.
- Chauvel, C., Lewin, E., Carpentier, M., Arndt, N.T., and Marini, J.C., 2008, Role of recycled oceanic basalt and sediment in generating the Hf–Nd mantle array: *Nature Geoscience*, v. 1, p. 64–67, <https://doi.org/10.1038/ngeo.2007.51>.
- Chen, Y., Huang, F., Shi, G.H., Wu, F.Y., Chen, X., Jin, Q.Z., Su, B., Guo, S., Sein, K., and Nyunt, T.T., 2018, Magnesium isotope composition of subduction zone fluids as constrained by jadeitites from Myanmar: *Journal of Geophysical Research: Solid Earth*, v. 123, p. 7566–7585, <https://doi.org/10.1029/2018JB015805>.
- Codillo, E.A., Le Roux, V., and Marschall, H.R., 2018, Arc-like magmas generated by mélange-peridotite interaction in the mantle wedge: *Nature Communications*, v. 9, no. 2864, p. 1–11, <https://doi.org/10.1038/s41467-018-05313-2>.
- Cruz-Uribe, A.M., Marschall, H.R., Gaetani, G.A., and Le Roux, V., 2018, Generation of alkaline magmas in subduction zones by partial melting of mélange diapirs: An experimental study: *Geology*, v. 46, p. 343–346, <https://doi.org/10.1130/G39956.1>.
- Currie, C.A., and Hyndman, R.D., 2006, The thermal structure of subduction zone back arcs: *Journal of Geophysical Research: Solid Earth*, v. 111, <https://doi.org/10.1029/2005JB004024>.
- Donoghue, E., Troll, V.R., Harris, C., O'Halloran, A., Walter, T.R., and Torrado, F.J.P., 2008, Low-temperature hydrothermal alteration of intra-caldera tuffs, Miocene Tejeda caldera, Gran Canaria, Canary Islands: *Journal of Volcanology and Geothermal Research*, v. 176, p. 551–564, <https://doi.org/10.1016/j.jvolgeores.2008.05.002>.
- Fritzell, E.H., Bull, A.L., and Shephard, G.E., 2016, Closure of the Mongol-Okhotsk Ocean: Insights from seismic tomography and numerical modelling: *Earth and Planetary Science Letters*, v. 445, p. 1–12, <https://doi.org/10.1016/j.epsl.2016.03.042>.
- Gerya, T.V., and Yuen, D.A., 2003, Characteristics-based marker-in-cell method with conservative finite-differences schemes for modeling geological flows with strongly variable transport properties: *Physics of the Earth and Planetary Interiors*, v. 140, p. 293–318, <https://doi.org/10.1016/j.pepi.2003.09.006>.
- Gerya, T.V., and Yuen, D.A., 2007, Robust characteristics method for modelling multiphase visco-elasto-plastic thermo-mechanical problems: *Physics of the Earth and Planetary Interiors*, v. 163, p. 83–105, <https://doi.org/10.1016/j.pepi.2007.04.015>.
- Hanchar, J.M., and Miller, C.F., 1993, Zircon zonation patterns as revealed by cathodoluminescence and backscattered electron images: Implications for interpretation of complex crustal histories: *Chemical Geology*, v. 110, p. 1–13, [https://doi.org/10.1016/0009-2541\(93\)90244-D](https://doi.org/10.1016/0009-2541(93)90244-D).
- Hao, L.L., Nan, X.Y., Kerr, A.C., Li, S.Q., Wu, Y.B., Wang, H., and Huang, F., 2022, Mg–Ba–Sr–Nd isotopic evidence for a mélange origin of early Paleozoic arc magmatism: *Earth and Planetary Science Letters*, v. 577, <https://doi.org/10.1016/j.epsl.2021.117263>.
- Hart, S.R., Gerlach, D.C., and White, W.M., 1986, A possible new Sr–Nd–Pb mantle array and consequences for mantle mixing: *Geochimica et Cosmochimica Acta*, v. 50, p. 1551–1557, [https://doi.org/10.1016/0016-7037\(86\)90329-7](https://doi.org/10.1016/0016-7037(86)90329-7).
- Hawkesworth, C.J., and Kemp, A.I.S., 2006, Evolution of the continental crust: *Nature*, v. 443, p. 811–817, <https://doi.org/10.1038/nature05191>.
- Hermann, J., and Rubatto, D., 2009, Accessory phase control on the trace element signature of sediment melts in subduction zones: *Chemical Geology*, v. 265, p. 512–526, <https://doi.org/10.1016/j.chemgeo.2009.05.018>.
- Ho, C.Q., 2019, Conditions of mélange diapir formation [B.S. thesis]: College Park, Maryland, University of Maryland, 28 p.
- Hofmann, A.W., 1997, Mantle geochemistry: The message from oceanic volcanism: *Nature*, v. 385, p. 219–229, <https://doi.org/10.1038/385219a0>.
- Hu, Y., Teng, F.Z., Plank, T., and Huang, K.J., 2017, Magnesium isotopic composition of subducting marine sediments: *Chemical Geology*, v. 466, p. 15–31, <https://doi.org/10.1016/j.chemgeo.2017.06.010>.
- Huang, K.J., Teng, F.Z., Plank, T., Staudigel, H., Hu, Y., and Bao, Z.Y., 2018, Magnesium isotopic composition of altered oceanic crust and the global Mg cycle: *Geochimica et Cosmochimica Acta*, v. 238, p. 357–373, <https://doi.org/10.1016/j.gca.2018.07.011>.
- IMBGM (Inner Mongolian Bureau of Geology Mineral Resources), 1991, *Regional Geology of Inner Mongolia*: Beijing, China, Geological Publishing House, 725 p. [in Chinese with English abstract].
- Jahn, B.M., Wu, F.Y., and Chen, B., 2000, Massive granitoid generation in Central Asia: Nd isotope evidence and implication for continental growth in the Phanerozoic: *Episodes*, v. 23, p. 82–92, <https://doi.org/10.18814/epiquery/2000/v23/001>.
- Kelley, K.A., Plank, T., Newman, S., Stolper, E.M., Grove, T.L., Parman, S., and Hauri, E.H., 2010, Mantle melting as a function of water content beneath the Mariana Arc: *Journal of Petrology*, v. 51, p. 1711–1738, <https://doi.org/10.1093/petrology/egq036>.
- Lin, C.H., Shih, M.H., and Lai, Y.C., 2021, Mantle wedge diapirs detected by a dense seismic array in Northern Taiwan: *Scientific Reports*, v. 11, 1561, p. 1–12, <https://doi.org/10.1038/s41598-021-81357-7>.
- Little, T.A., Hacker, B.R., Gordon, S.M., Baldwin, S.L., Fitzgerald, P.G., Ellis, S., and Korchinski, M., 2011, Diapiric exhumation of Earth's youngest (UHP) eclogites in the gneiss domes of the D'Entrecasteaux Islands, Papua New Guinea: *Tectonophysics*, v. 510, p. 39–68, <https://doi.org/10.1016/j.tecto.2011.06.006>.
- Liu, H.C., Li, Y.L., He, H.Y., Huangfu, P.P., and Liu, Y.Z., 2018, Two-phase southward subduction of the Mongol-Okhotsk oceanic plate constrained by Permian–Jurassic granitoids in the Erguna and Xing'an massifs (NE China): *Lithos*, v. 304–307, p. 347–361, <https://doi.org/10.1016/j.lithos.2018.01.016>.
- Liu, H.C., Li, Y.L., Wu, L.W., Huangfu, P.P., and Zhang, M., 2019, Geochemistry of high-Nb basalt-andesite in the Erguna Massif (NE China) and implications for the early Cretaceous back-arc extension: *Geological Journal*, v. 54, p. 291–307, <https://doi.org/10.1002/gj.3176>.
- Liu, P.P., Teng, F.Z., Dick, H.J.B., Zhou, M.F., and Chung, S.L., 2017, Magnesium isotopic composition of the oceanic mantle and oceanic Mg cycling: *Geochimica et Cosmochimica Acta*, v. 206, p. 151–165, <https://doi.org/10.1016/j.gca.2017.02.016>.
- Nielsen, S.G., and Marschall, H.R., 2017, Geochemical evidence for mélange melting in global arcs: *Science Advances*, v. 3, p. 1–6, <https://doi.org/10.1126/sciadv.1602402>.
- Petford, N., Cruden, A.R., McCaffrey, K.J.W., and Vigneresse, J.L., 2000, Granite magma formation, transport and emplacement in the Earth's crust: *Nature*, v. 408, p. 669–673, <https://doi.org/10.1038/35047000>.
- Pilet, S., Baker, M.B., and Stolper, E.M., 2008, Metasomatized lithosphere and the origin of alkaline lavas: *Science*, v. 320, p. 916–919, <https://doi.org/10.1126/science.1156563>.
- Plank, T., Kelley, K.A., Murray, R.W., and Stern, L.Q., 2007, Chemical composition of sediments subducting at the Izu-Bonin trench: *Geochemistry, Geophysics, Geosystems*, v. 8, p. 1–16, <https://doi.org/10.1029/2006GC001444>.
- Rapp, R.P., Shimizu, N., and Norman, M.D., 2003, Growth of early continental crust by partial melting of eclogite: *Nature*, v. 425, p. 605–609, <https://doi.org/10.1038/nature02031>.
- Rudnick, R.L., 1995, Making continental-crust: *Nature*, v. 378, p. 571–578, <https://doi.org/10.1038/378571a0>.
- Ruppen, D., Knaf, A., Bussien, D., Winkler, W., Chimedtsere, A., and von Quadt, A., 2014, Restoring the Silurian to Carboniferous northern active continental margin of the Mongol-Okhotsk Ocean in Mongolia: Hangay-Hentey accretionary wedge and seamount collision: *Gondwana Research*, v. 25, p. 1517–1534, <https://doi.org/10.1016/j.gr.2013.05.022>.
- Rutter, S., Nebel, O., Nebel-Yacobsen, Y., Cohen, B.E., and Eggins, S., 2021, Alkalinity of ocean island lavas decoupled from enriched source components: A case study from the EM1-PREMA Tasmanid mantle plume: *Geochimica et Cosmochimica Acta*, v. 314, p. 140–158, <https://doi.org/10.1016/j.gca.2021.09.023>.
- Şengör, A.M.C., Natal'in, B.A., Sunal, G., and van der Voo, R., 2018, The tectonics of the Altaids: Crustal growth during the construction of the continental lithosphere of Central Asia between ~750 and ~130 Ma ago: *Annual Review of Earth and Planetary Sciences*, v. 46, p. 439–494, <https://doi.org/10.1146/annurev-earth-060313-054826>.
- Sobolev, A.V., Hofmann, A.W., Jochum, K.P., Kuzmin, D.V., and Stoll, B., 2011, A young source for the Hawaiian plume: *Nature*, v. 476, p. 434–437, <https://doi.org/10.1038/nature10321>.
- Staudigel, H.G.R., Davies, S.R., Hart, K., Marchant, M., and Smith, B.M., 1995, Large-scale isotopic Sr, Nd and O isotopic anatomy of altered oceanic crust: DSDP/ODP sites 417/418: *Earth and Planetary Science Letters*, v. 130, p. 169–185, [https://doi.org/10.1016/0012-821X\(94\)00263-X](https://doi.org/10.1016/0012-821X(94)00263-X).
- Tang, Y.J., Zhang, H.F., and Ying, J.F., 2010, A brief review of isotopically light Li: A feature of the enriched mantle?: *International Geology Review*, v. 52, p. 964–976, <https://doi.org/10.1080/00206810903211385>.
- Teng, F.Z., Hu, Y., and Chauvel, C., 2016, Magnesium isotope geochemistry in arc volcanism: Proceedings of the National Academy of Sciences of the United States of America, v. 113, p. 7082–7087, <https://doi.org/10.1073/pnas.1518456113>.
- Tomurtogoo, O., Windley, B.F., Kroner, A., Badarch, G., and Liu, D.Y., 2005, Zircon age and occurrence of the Adatsag ophiolite and Muro shear zone, central Mongolia: Constraints on the evolution of the Mongol-

- Okhotsk ocean, suture and orogen: *Journal of the Geological Society*, v. 162, p. 125–134, <https://doi.org/10.1144/0016-764903-146>.
- Troch, J., Ellis, B.S., Harris, C., Bachmann, O., and Bindeman, I.N., 2020, Low-delta O-18 silicic magmas on Earth: A review: *Earth-Science Reviews*, v. 208, <https://doi.org/10.1016/j.earscirev.2020.103299>.
- Vervoort, J.D., Plank, T., and Prytulak, J., 2011, The Hf-Nd isotopic composition of marine sediments: *Geochimica et Cosmochimica Acta*, v. 75, p. 5903–5926, <https://doi.org/10.1016/j.gca.2011.07.046>.
- Wang, W.Z., Zhou, C., Liu, Y., Wu, Z.Q., and Huang, F., 2019, Equilibrium Mg isotope fractionation among aqueous Mg²⁺, carbonates, brucite and lizardite: Insights from first-principles molecular dynamics simulations: *Geochimica et Cosmochimica Acta*, v. 250, p. 117–129, <https://doi.org/10.1016/j.gca.2019.01.042>.
- Weaver, B.L., 1991, The origin of ocean island basalt end-member compositions: Trace element and isotopic constraints: *Earth and Planetary Science Letters*, v. 104, p. 381–397, [https://doi.org/10.1016/0012-821X\(91\)90217-6](https://doi.org/10.1016/0012-821X(91)90217-6).
- Wu, F., Turner, S., and Schaefer, B.F., 2020, Melange versus fluid and melt enrichment of subarc mantle: A novel test using barium isotopes in the Tonga-Kermadec arc: *Geology*, v. 48, p. 1053–1057, <https://doi.org/10.1130/G47549.1>.
- Xiao, W.J., Windley, B.F., Sun, S., Li, J.L., Huang, B.C., Han, C.M., Yuan, C., Sun, M., and Chen, H.L., 2015, A tale of amalgamation of three Permo-Triassic collage systems in Central Asia: Oroclines, sutures, and terminal accretion: *Annual Review of Earth and Planetary Sciences*, v. 43, p. 477–507, <https://doi.org/10.1146/annurev-earth-060614-105254>.
- Xu, B., Griffin, W.L., Xiong, Q., Hou, Z.Q., O'Reilly, S.Y., Guo, Z., Pearson, N.J., Greau, Y., Yang, Z.M., and Zheng, Y.C., 2017, Ultrapotassic rocks and xenoliths from South Tibet: Contrasting styles of interaction between lithospheric mantle and asthenosphere during continental collision: *Geology*, v. 45, p. 51–54, <https://doi.org/10.1130/G38466.1>.
- Xu, Y.G., Chung, S.L., Jahn, B.M., and Wu, G.Y., 2001, Petrologic and geochemical constraints on the petrogenesis of Permian-Triassic Emeishan flood basalts in southwestern China: *Lithos*, v. 58, p. 145–168, [https://doi.org/10.1016/S0024-4937\(01\)00055-X](https://doi.org/10.1016/S0024-4937(01)00055-X).
- Xu, Y.G., Ma, J.L., Frey, F.A., Feigenson, M.D., and Liu, J.F., 2005, Role of lithosphere-asthenosphere interaction in the genesis of Quaternary alkali and tholeiitic basalts from Datong, western North China Craton: *Chemical Geology*, v. 224, p. 247–271, <https://doi.org/10.1016/j.chemgeo.2005.08.004>.
- Zack, T., Tomascak, P.B., Rudnick, R.L., Dalpe, C., and McDonough, W.F., 2003, Extremely light Li in orogenic eclogites: The role of isotope fractionation during dehydration in subducted oceanic crust: *Earth and Planetary Science Letters*, v. 208, p. 279–290, [https://doi.org/10.1016/S0012-821X\(03\)00035-9](https://doi.org/10.1016/S0012-821X(03)00035-9).
- Zhang, C., Liu, L.F., Santosh, M., Luo, Q., and Zhang, X., 2017, Sediment recycling and crustal growth in the Central Asian Orogenic Belt: Evidence from Sr-Nd-Hf isotopes and trace elements in granitoids of the Chinese Altay: *Gondwana Research*, v. 47, p. 142–160, <https://doi.org/10.1016/j.gr.2016.08.009>.
- Zhang, C., Santosh, M., Liu, L.F., Luo, Q., Zhang, X., and Liu, D.D., 2018, Early Silurian to Early Carboniferous ridge subduction in NW Junggar: Evidence from geochronological, geochemical, and Sr-Nd-Hf isotopic data on alkali granites and adakites: *Lithos*, v. 300–301, p. 314–329, <https://doi.org/10.1016/j.lithos.2017.12.010>.
- Zhang, C., Liu, D., Zhang, X., Spencer, C., Tang, M., Zeng, J., Jiang, S., Jolivet, M., and Kong, X., 2020, Hafnium isotopic disequilibrium during sediment melting and assimilation: *Geochemical Perspectives Letters*, v. 12, p. 34–39, <https://doi.org/10.7185/geochemlet.2001>.
- Zhang, K.J., 2014, Genesis of the Late Mesozoic Great Xing'an Range Large Igneous Province in eastern central Asia: A Mongol-Okhotsk slab window model: *International Geology Review*, v. 56, p. 1557–1583, <https://doi.org/10.1080/00206814.2014.946541>.
- Zhao, Z.F., and Zheng, Y.F., 2003, Calculation of oxygen isotope fractionation in magmatic rocks: *Chemical Geology*, v. 193, p. 59–80, [https://doi.org/10.1016/S0009-2541\(02\)00226-7](https://doi.org/10.1016/S0009-2541(02)00226-7).
- Zhong, Y., Chen, L.H., Wang, X.J., Zhang, G.L., Xie, L.W., and Zeng, G., 2017, Magnesium isotopic variation of oceanic island basalts generated by partial melting and crustal recycling: *Earth and Planetary Science Letters*, v. 463, p. 127–135, <https://doi.org/10.1016/j.epsl.2017.01.040>.
- Zhu, Y.S., Yang, J.H., Sun, J.F., and Wang, H., 2017, Zircon Hf-O isotope evidence for recycled oceanic and continental crust in the sources of alkaline rocks: *Geology*, v. 45, p. 407–410, <https://doi.org/10.1130/G38872.1>.

SCIENCE EDITOR: WENJIAO XIAO
ASSOCIATE EDITOR: CHANGQING YIN

MANUSCRIPT RECEIVED 28 JANUARY 2023
REVISED MANUSCRIPT RECEIVED 6 MAY 2023
MANUSCRIPT ACCEPTED 27 MAY 2023

Printed in the USA